ADVANCED FUNCTIONAL MATERIALS
www.afm-journal.de

# Electrical Interrogation of Thickness-Dependent Multiferroic Phase Transitions in the 2D Antiferromagnetic Semiconductor $NiI_2$

*Dmitry Lebedev, Jonathan Tyler Gish, Ethan Skyler Garvey, Teodor Kosev Stanev, Junhwan Choi, Leonidas Georgopoulos, Thomas Wei Song, Hong Youl Park, Kenji Watanabe, Takashi Taniguchi, Nathaniel Patrick Stern, Vinod Kumar Sangwan, and Mark Christopher Hersam**

**2D magnetic materials hold promise for quantum and spintronic applications. 2D antiferromagnetic materials are of particular interest due to their relative insensitivity to external magnetic fields and higher switching speeds compared to 2D ferromagnets. However, their lack of macroscopic magnetization impedes detection and control of antiferromagnetic order, thus motivating magneto-electrical measurements for these purposes. Additionally, many 2D magnetic materials are ambient-reactive and electrically insulating or highly resistive below their magnetic ordering temperatures, which imposes severe constraints on electronic device fabrication and characterization. Herein, these issues are overcome via a fabrication protocol that achieves electrically conductive devices from the ambient-reactive 2D antiferromagnetic semiconductor $NiI_2$. The resulting gate-tunable transistors show band-like electronic transport below the antiferromagnetic and multiferroic transition temperatures of $NiI_2$, revealing a Hall mobility of 15 $cm^2 V^{-1} s^{-1}$ at 1.7 K. These devices also allow direct electrical probing of the thickness-dependent multiferroic phase transition temperature of $NiI_2$ from 59 K (bulk) to 28 K (monolayer).**

## 1. Introduction

2D van der Waals magnetic and ferroelectric (FE) materials have attracted significant attention for advanced applications including low-power logic and memory switches.[1,2] Moreover, 2D FE materials have shown layer-dependent ferroelectricity[3,4] and FE switching of a 2D metal,[5] while 2D magnetic materials have demonstrated thickness-dependent and stacking-dependent magnetic order,[6,7] electrically controlled magnetism,[8,9] and giant tunneling magnetoresistance.[10] However, the majority of 2D magnets order antiferromagnetically.[2] While antiferromagnetic (AFM) materials are more robust against external parasitic magnetic fields and enable higher operating frequencies compared to ferromagnets, their lack of macroscopic magnetization limits detection and control of AFM order.[11] For example,

D. Lebedev, J. T. Gish, J. Choi, L. Georgopoulos, T. W. Song, H. Y. Park, V. K. Sangwan, M. C. Hersam
Department of Materials Science and Engineering
Northwestern University
Evanston, IL 60208, USA
E-mail: m-hersam@northwestern.edu

E. S. Garvey, T. K. Stanev, N. P. Stern
Department of Physics and Astronomy
Northwestern University
Evanston, IL 60208, USA

The ORCID identification number(s) for the author(s) of this article can be found under https://doi.org/10.1002/adfm.202212568.



**DOI: 10.1002/adfm.202212568**

K. Watanabe
Research Center for Functional Materials
National Institute for Materials Science
1-1 Namiki, Tsukuba 305-0044, Japan

T. Taniguchi
International Center for Materials Nanoarchitectonics
National Institute for Materials Science
1-1 Namiki, Tsukuba 305-0044, Japan

M. C. Hersam
Department of Chemistry
Northwestern University
Evanston, IL 60208, USA

M. C. Hersam
Department of Electrical and Computer Engineering
Northwestern University
Evanston, IL 60208, USA

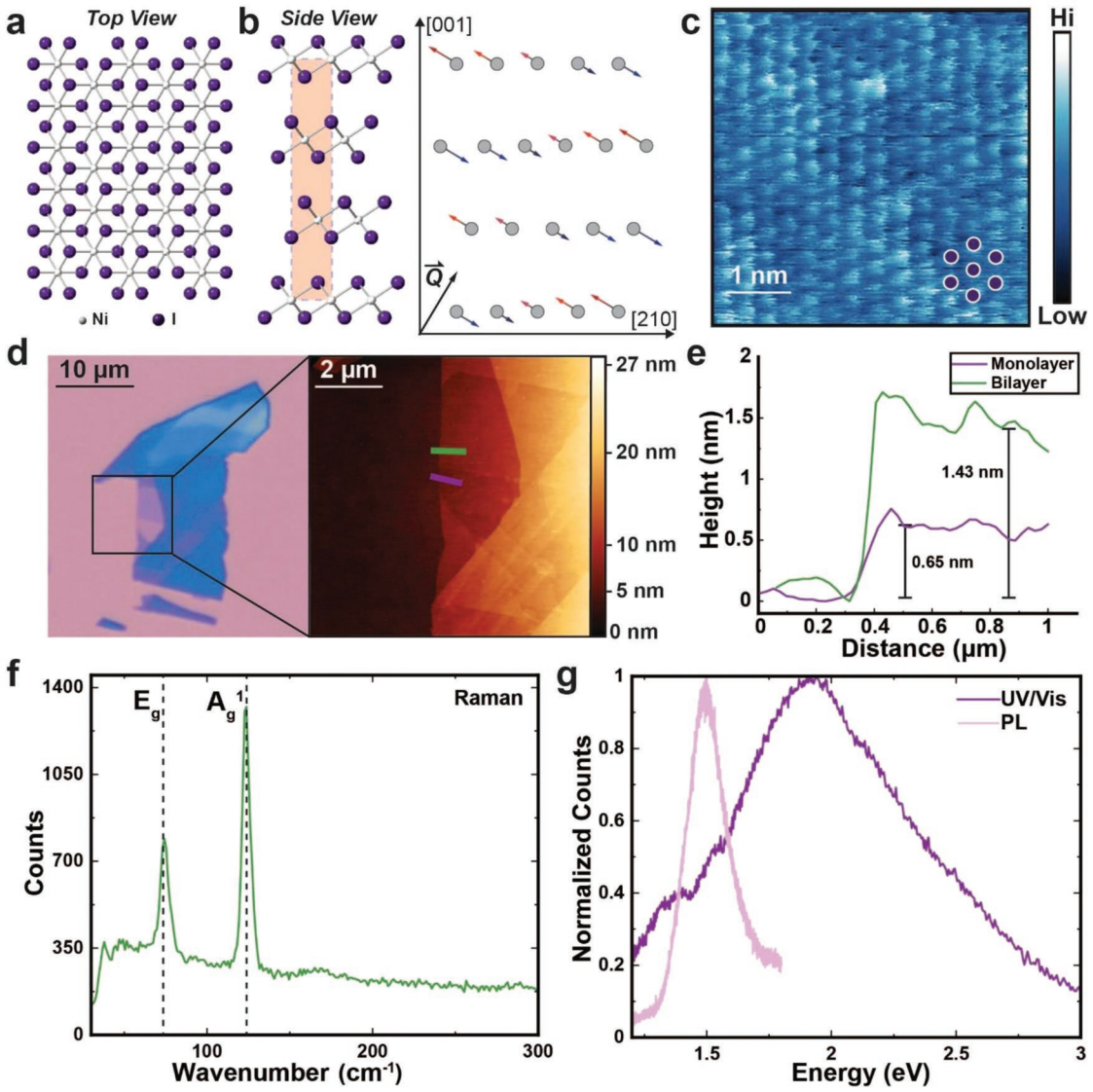


**Figure 1.** a) Top and b) side view on the crystal structure of $NiI_2$ ($CdCl_2$-type). b) Schematic of the helical ground state magnetic order of $NiI_2$ below $T_{N2}$: spins are perpendicular to $Q \approx (0.138,0,1.457)$. c) Ultrahigh vacuum scanning tunneling microscopy image of $NiI_2$, taken at 200 mV sample bias and 0.9 nA tunneling current, reveals a hexagonal lattice with a periodicity of 0.40 nm as expected for $NiI_2$. d) Optical and atomic force microscopy images with e) extracted height profiles corresponding to monolayer and bilayer regions. f) Raman spectroscopy of bulk $NiI_2$ at room temperature. g) Photoluminescence and absorption spectra of bulk $NiI_2$ at room temperature.

common techniques for studying AFM materials, such as X-ray magnetic dichroism and neutron scattering, are exceptionally challenging to apply to microcrystals and 2D flakes.[2]

Alternatively, charge transport characterization is preferable for detecting and manipulating AFM order since it can be straightforwardly applied on nanoscale samples and enables AFM device integration with peripheral electrical circuits. In addition, spin-dependent charge transport measurements allow additional options for coupling magnetic and electronic phenomena, such as magnetoresistance and spin-orbit torque, providing further motivation for electrically probing 2D magnetic materials.[11] However, since most 2D magnetic materials are chemically unstable in ambient conditions, electronic device fabrication is cumbersome, which constrains accessible architectures. Furthermore, most 2D magnetic materials show undetectably low charge transport below their magnetic ordering temperatures, which is often attributed to carrier localization,[12,13] but may also result from poor charge injection due to chemical reactions with electrode materials. Consequently, previous attempts at 2D AFM electrical transport measurements have been limited to vertical device geometries, where the 2D AFM layers act solely as tunneling barriers.[8–10,14]

$NiI_2$ is an emerging 2D AFM material, whose structure consists of layers of edge-sharing [$NiI_6$] octahedra that are separated by van der Waals gaps (**Figure 1**a,b). Chemically, $NiI_2$ is highly hygroscopic, resulting in rapid degradation in ambient conditions.[15] In the bulk, $NiI_2$ is a Mott-insulator,[16] which exhibits both long-range magnetic ordering and spontaneous

electrical polarization, known as multiferroicity.[17] Bulk $NiI_2$ undergoes two antiferromagnetic transitions at $T_{N1} = 76$ K and $T_{N2} = 59$ K, with helical AFM ground state magnetic ordering along the propagation vector **Q** (Figure 1b).[18] While $NiI_2$ has a centrosymmetric $CdCl_2$-type crystal structure at room temperature, the emerging magnetic order at the $T_{N2}$ transition breaks inversion symmetry and drives in-plane ferroelectricity due to strong Dzyaloshinskii–Moriya interactions.[19] Recently, this multiferroicity was detected down to the monolayer limit for $NiI_2$ via optical measurements.[19] Since the optical absorption spectrum of $NiI_2$ possesses an excitonic peak at 1.38 eV[20] and the width of the conduction band is estimated at ≈1 eV,[21] $NiI_2$ is expected to show gate-tunable semiconducting electronic transport over a broad temperature range. However, likely due to complications arising from its high chemical reactivity, variable-temperature charge transport measurements below the multiferroic transition temperature of atomically thin $NiI_2$ have not yet been reported.

Here, we combine a dry flake transfer method with atomic layer deposition (ALD) to fabricate multi-terminal electrical devices from exfoliated $NiI_2$. This fabrication protocol results in ambient-stable electrical contacts to $NiI_2$ that enable charge transport measurements at cryogenic temperatures. In this manner, we confirm that $NiI_2$ is a gate-tunable semiconductor down to monolayer thickness with band-like transport and a Hall mobility of 15 $cm^2\ V^{-1}\ s^{-1}$ at a temperature of 1.7 K. Variable-temperature magnetotransport measurements further reveal an anisotropic magnetoresistance of $NiI_2$, which changes sign at $T_{N2}$, likely associated with strong spin-orbit coupling. These magnetotransport measurements allow the onset of multiferroicity to be electrically probed, thereby enabling the thickness dependence of $T_{N2}$ to be measured from 59 K in bulk $NiI_2$ to 28 K in monolayer $NiI_2$, which is consistent with significant interlayer exchange interactions in $NiI_2$.[6,19]

## 2. Results and Discussion

$NiI_2$ crystals were prepared using the chemical vapor transport (CVT) method from elemental sources. Ultrahigh vacuum (UHV) scanning tunneling microscopy (STM) at room temperature revealed a hexagonal lattice with a periodicity of 0.40 nm (Figure 1c), consistent with the $NiI_2$ crystal structure ($a$ = 0.392 nm).[18] The $NiI_2$ crystal was micromechanically exfoliated in an inert-atmosphere $N_2$ glovebox, where few-layer flakes were identified optically. The optical contrast of the resulting $NiI_2$ flakes was correlated with thickness using inert-atmosphere atomic force microscopy (Figure 1d,e and Figure S1, Supporting Information). $NiI_2$ flakes were encapsulated with 55 nm of alumina grown by ALD (Figure S1, Supporting Information),[22] which enabled ambient Raman, photoluminescence (PL), and optical absorption measurements (Figure 1f,g) that are consistent with previous literature reports.[15,19,20] To confirm the ferroelectricity of $NiI_2$, second harmonic generation and linear dichroism measurements were performed, which confirmed the existence of in-plane polarization in $NiI_2$ below $T_{N2}$ (Figure S2, Supporting Information).

To develop the device fabrication protocol, we first studied the stability of exfoliated $NiI_2$ flakes in air and in different solvents commonly used for flake transfer and lithographic processes (e.g., acetone and chloroform). Unprotected $NiI_2$ flakes were found to degrade in air and chloroform over the course of hours (**Figure 2**). Monolayers of $NiI_2$ even degrade in an inert atmosphere ($N_2$ glovebox) within a few days when in contact with tape residue (Figure S3, Supporting Information), further emphasizing the need for effective passivation. In contrast, we find that 1,2-dichloroethane (1,2-DCE) does not degrade $NiI_2$ (Figure S4, Supporting Information). Hence, 1,2-DCE was used as the solvent for subsequent device fabrication.

$NiI_2$ devices were assembled via a dry pick-up and transfer method using few-layer hexagonal boron nitride (hBN) to sandwich $NiI_2$ flakes, which provided a well-defined dielectric environment for charge transport measurements (see Experimental Section for details). In addition, few-layer graphene was used as electrical contacts since its chemical inertness minimizes the chance of unwanted interfacial reactions at $NiI_2$ contacts. Fabricating $NiI_2$ field-effect transistors (FETs) down to monolayer thickness presents another challenge as large few-layer flakes are often connected to thicker (>20 nm) flakes (**Figure 3**a and Figures S5 and S6, Supporting Information). Therefore, a PC/PDMS (polydimethylsiloxane) polymer stamp was used to sequentially remove surrounding thicker $NiI_2$ flakes, while keeping the few-layer $NiI_2$ flakes intact (Figure 3a–c). If left unremoved, large neighboring $NiI_2$ flakes prevent homogeneous contact between the top hBN and few-layer $NiI_2$, resulting in tearing, folding, and/or formation of bubbles trapped at the interface during the stamping process, all of which negatively affect electrical transport. Overall, this procedure enables the fabrication of high-quality $NiI_2$ FETs with semiconducting channels of different thicknesses (Figure S6, Supporting Information).

To achieve multi-terminal devices, the hBN/graphene/$NiI_2$/hBN heterostructures were patterned using electron-beam lithography followed by reactive ion etching (RIE) (see Experimental Methods for details and Figure 3d,e). It should be noted that RIE exposes the edges of the semiconducting material in the heterostructure stack, which has limited this procedure to ambient-stable 2D semiconductors in the past.[23] Indeed, $NiI_2$ flakes with exposed edges degrade in both ambient conditions and acetone (Figure 2c,d), similar to unprotected flakes. Charge transport in transition metal halides is highly sensitive to chemical degradation, with FET electrical characteristics decaying irreversibly even for flakes that appear optically intact.[22] To avoid this degradation, the resist was stripped using 1,2-DCE, and then the entire hBN/graphene/$NiI_2$/hBN stack was encapsulated with 55 nm of ALD alumina. In this manner, the final device structures were stable in ambient conditions, which allowed for handling in air for wire bonding, as well as electrical and optical measurements (Figure 3f and Figure S7, Supporting Information).

The resulting devices reveal that $NiI_2$ is a gate-tunable, ambipolar semiconductor with electron (hole) field-effect mobilities of ≈1 $cm^2\ V^{-1}\ s^{-1}$ (0.01 $cm^2\ V^{-1}\ s^{-1}$) and on/off ratios of $10^5$ ($10^3$) at room temperature (**Figure 4**a). Temperature-dependent charge transport measurements with a back-gate voltage $V_G$ = 60 V revealed a clear peak in resistance at $T_{N2}$ = 59 K for bulk $NiI_2$, which corresponds to the helical magnetic and structural transition of $NiI_2$, as well as the onset of the

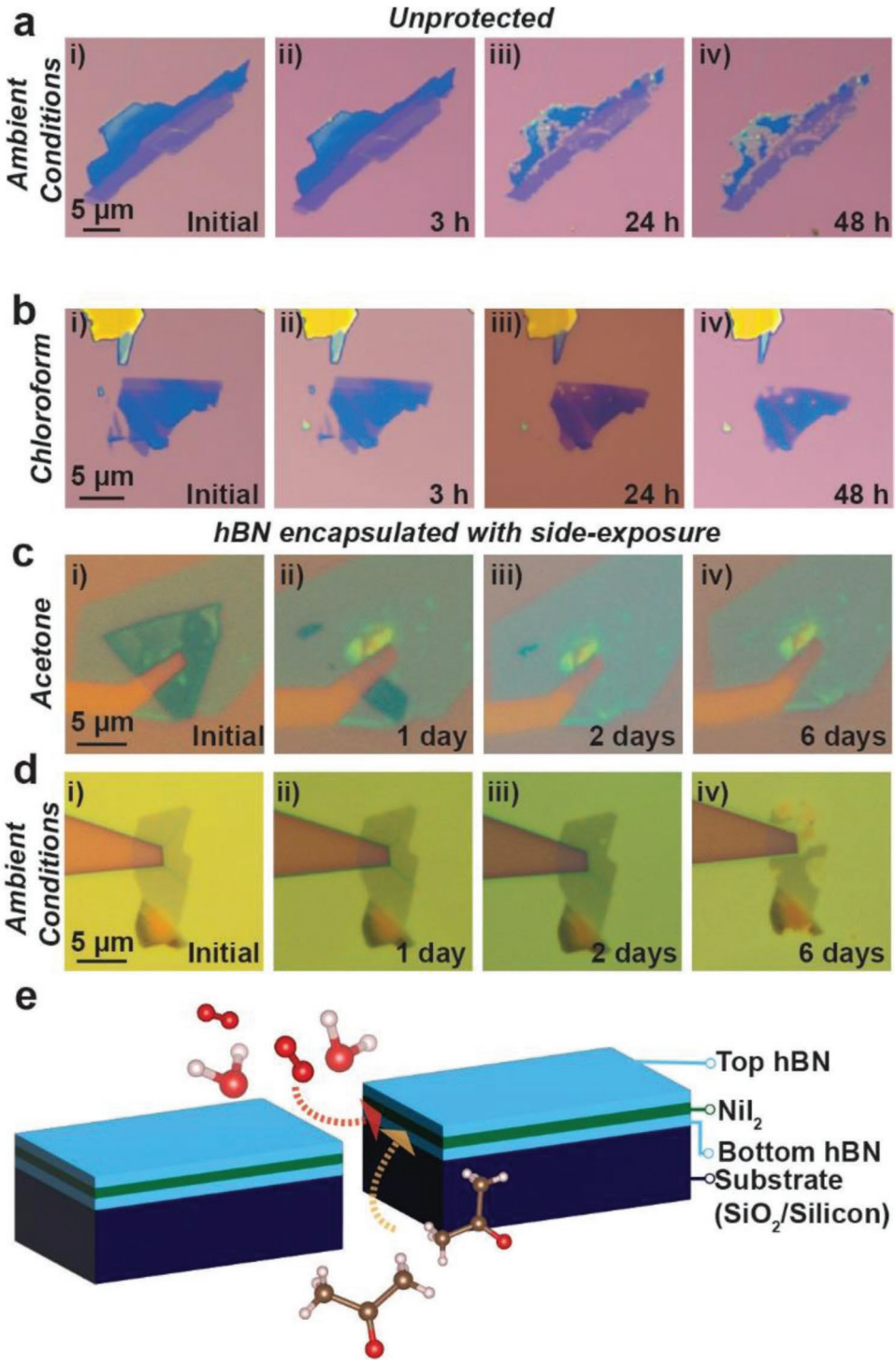


**Figure 2.** a,b) Degradation of unprotected $NiI_2$ flakes in ambient atmosphere and chloroform, respectively. c,d) Edge-initiated degradation of an etched hBN/$NiI_2$/hBN stack in acetone and ambient atmosphere, respectively. e) Schematic of the etched hBN/$NiI_2$/hBN stack with the edge exposed to ambient species and/or solvents.

multiferroic order (Figure 4b).[18,24] Plotting ln(R) versus inverse T shows a kink at 76 K (inset of Figure 4b), which corresponds to $T_{N1}$ of bulk $NiI_2$.[18,24] Moreover, photocurrent measurements reveal the bulk photovoltaic effect, which is induced by the spontaneous electrical polarization of ferroelectric materials, further confirming the multiferroic nature of $NiI_2$ below $T_{N2}$ (Figure S8, Supporting Information). The use of graphene contacts allowed electrical measurements down to 1.7 K, but the current–voltage characteristics became nonlinear at low temperatures (Figure S9, Supporting Information), which suggests

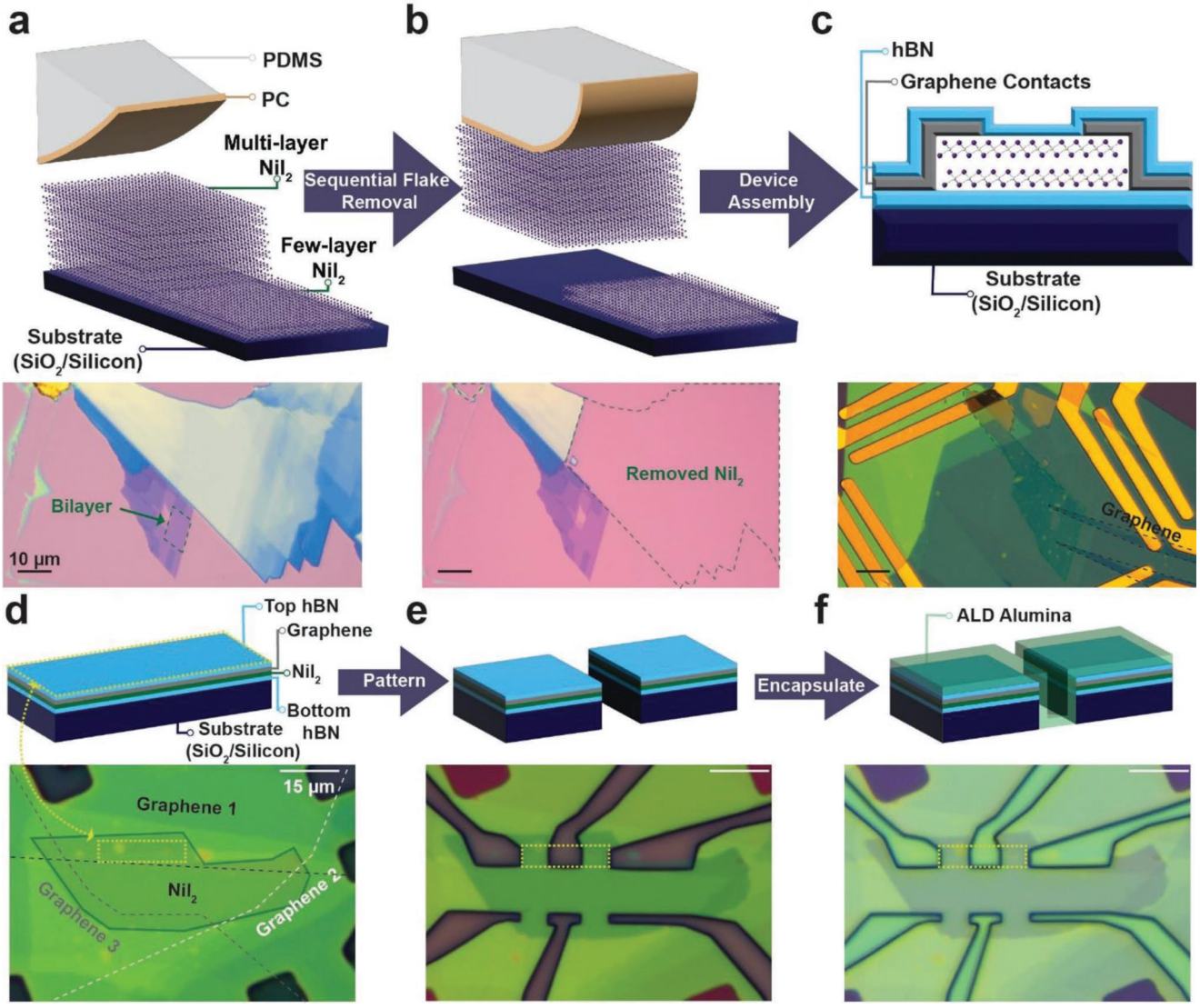


**Figure 3.** a,b) Schematic demonstrating removal of large and thick flakes preceding c) fabrication of few-layer $NiI_2$ electrical devices. Unless removed, thick $NiI_2$ flakes compromise the quality of the heterostructure due to large height differences that cause poor flake-to-flake contact and thus gas bubble incorporation. d–f) Schematic of the $NiI_2$ (>10 layers) Hall bar fabrication, which consists of flake pick-up and transfer to obtain the hBN/graphene/$NiI_2$/hBN stack, patterning and etching, and encapsulation via alumina atomic layer deposition. Although the graphene flakes are overlapping after the heterostructure assembly, subsequent etching defines the required Hall bar geometry.

a Schottky barrier is present that could potentially be resolved by subsequent contact engineering (e.g., electrostatic doping of contact regions). In contrast, direct metal contacts on $NiI_2$ FETs resulted in highly resistive devices with 100-fold lower mobility at low temperatures, thus illustrating the advantages of graphene contacts for $NiI_2$ (Figure S10, Supporting Information). To demonstrate low-voltage operation, we also fabricated local-gate $NiI_2$ FETs, which show on/off ratios of $10^5$ and operating voltages below 3 V both at room temperature and at 5 K (Figure S11, Supporting Information).

Electrical interrogation of the $NiI_2$ multiferroic transition facilitates thickness-dependent measurements of $T_{N2}$ down to the monolayer limit (Figure 4c,d). Even monolayer $NiI_2$ showed gate-tunable conductivity at low temperatures, although it was more resistive than thicker layers (Figure S9, Supporting Information). Electrical measurements revealed multiferroic transition temperatures of ≈28, 40, and 48 K for monolayer, bilayer, and trilayer $NiI_2$, respectively (Figure 4d and Figure S12, Supporting Information). These values are marginally higher than reports based on optical measurements,[15,19,25] which can likely be explained by differences in growth conditions and/or differing levels of ambient exposure. The strong thickness dependence of the multiferroic transition temperature indicates the presence of significant interlayer exchange interactions in $NiI_2$.[6,19]

To gain further insight into magnetotransport properties, Hall bars of several-layer $NiI_2$ were tested at temperatures above and below $T_{N2}$. Magnetoresistance is calculated based on four-probe ($R_{xx}$) measurements as $MR = \Delta R/R \times 100\% = (R_H - R_0)/R_0 \times 100\%$. With an out-of-plane magnetic field and $V_G = 60$ V,

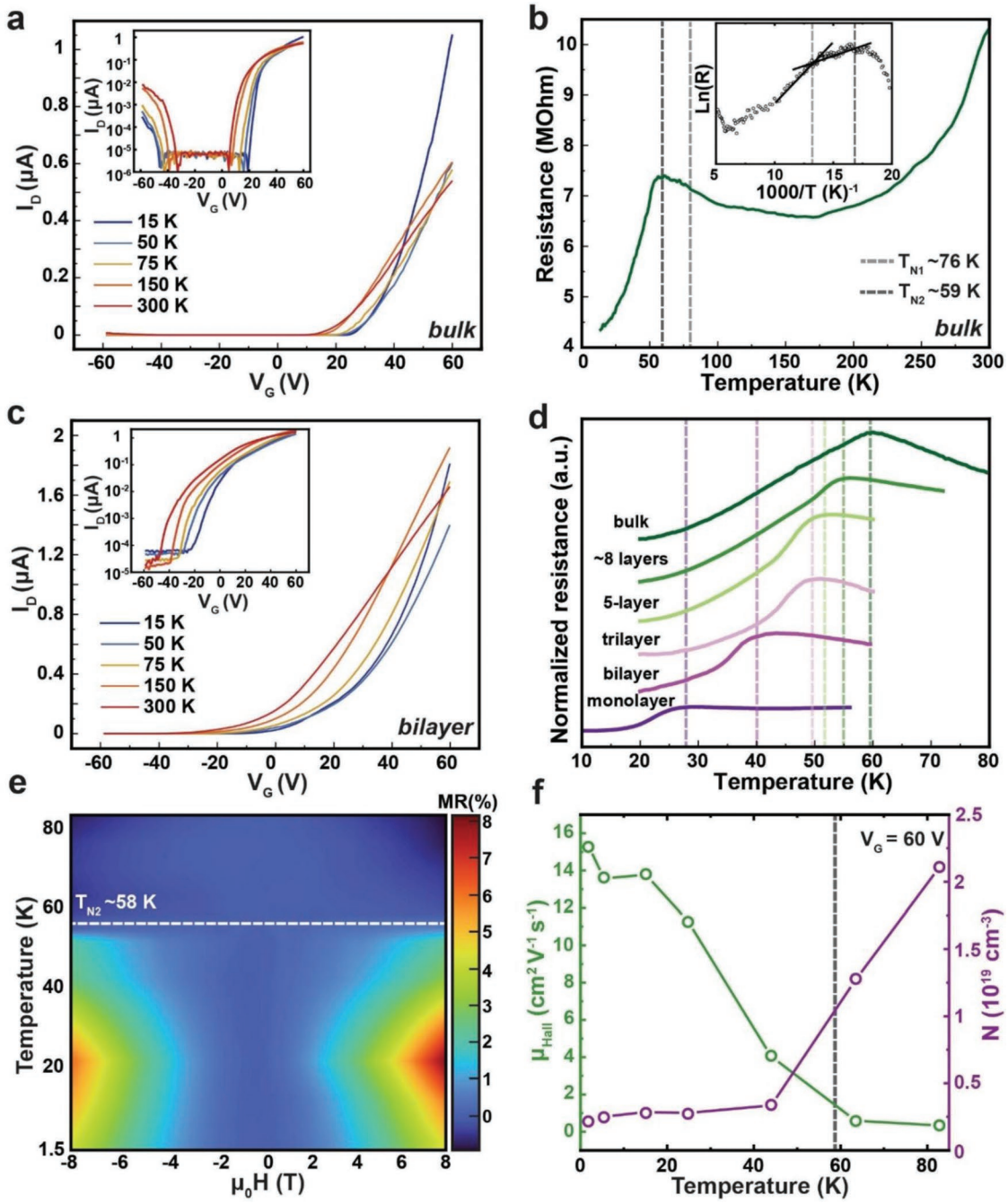


**Figure 4.** a) Transfer characteristics of a bulk $NiI_2$ FET at different temperatures ($V_D$ = 4 V) with the inset showing the same data on a log-linear scale. b) Resistance versus temperature of bulk $NiI_2$ FET ($V_G$ = 60 V, $V_D$ = 4 V) showing a peak at $T_{N2} \approx 59$ K and a kink at $T_{N1} \approx 76$ K (inset shows ln($R$) versus 1/$T$). c) Transfer characteristics of a bilayer $NiI_2$ FET at different temperatures ($V_D$ = 2 V) with the inset showing the same data on a log-linear scale. d) Resistance of various few-layer $NiI_2$ FETs versus temperature, showing a decrease of $T_{N2}$ with decreasing number of layers. e) Four-probe magnetoresistance and f) electron mobility and carrier concentration of bulk $NiI_2$ (>10 layers, shown in Figure 3f) at different temperatures, $V_G$ = 60 V.

a small (<1%) negative magnetoresistance was measured above $T_{N2}$, which can be assigned to field-induced suppression of electron scattering by magnetic fluctuations (Figure 4e).[12,26,27] At $T_{N2}$, the magnetoresistance changed sign to positive (Figure 4e and Figures S12 and S13, Supporting Information), and its magnitude increased with decreasing temperature, reaching 7% at 8 T and 1.7 K. The same trend was observed for the trilayer $NiI_2$, where the sign change occurred at lower temperature, in agreement with the lower $T_{N2}$ (46–50 K for trilayer $NiI_2$, Figure S14, Supporting Information). A positive magnetoresistance has recently been observed in layered AFM materials, such as CrSBr[12,26,27] and non-collinear $Co_{1/3}NbS_2$.[28] For both in-plane and out-of-plane orientations of the magnetic field, no kinks were observed in the magnetoresistance versus

magnetic field curves, which indicates that higher magnetic fields are needed to achieve spin-flip/spin-flop transitions in $NiI_2$. The magnetoresistance remained positive below $T_{N2}$ when the magnetic field was applied in-plane, and its magnitude was higher compared to the out-of-plane direction, reaching 12% at 8 T and 1.7 K (Figure S13, Supporting Information), implying significant magnetoresistive anisotropy. Anisotropic magnetoresistance has also been observed in the layered AFM material CrSBr, which was associated with spin-flip transitions and quasi-1D transport.[12,27] However, the anisotropic magnetoresistance of $NiI_2$ is more likely to be associated with large spin-orbit interactions.[19,29]

By fitting the transverse $R_{xy}$ data to the standard Hall effect model, the number of carriers at $V_G$ = 60 V decreased from $N \approx 2 \times 10^{19}$ cm$^{-3}$ at 83 K to $N \approx 3 \times 10^{18}$ cm$^{-3}$ below $T_{N2}$ and then did not vary significantly with further decreasing temperature (Figure 4f and Figure S13, Supporting Information). On the other hand, the Hall mobility increased at these low temperatures below $T_{N2}$, ultimately reaching 15 cm$^2$ V$^{-1}$ s$^{-1}$ at 1.7 K (Figure 4f and Figure S13, Supporting Information). By comparing the Hall mobilities with the field-effect mobilities extracted from the transistor data for the same device, we find that the Hall mobilities are approximately two times smaller (Figure S13, Supporting Information), which is most likely associated with the presence of localized states below the band edge.[30]

## 3. Conclusion

In summary, we have designed and implemented a protocol for fabricating electrical devices for ambient-reactive 2D $NiI_2$. These devices enable probing of the gate-tunable semiconducting properties of $NiI_2$ down to cryogenic temperatures, which allows extraction of the thickness dependence of the $NiI_2$ multiferroic phase transition down to the monolayer limit. This fabrication protocol also yields ambient-stable multi-terminal devices with a Hall mobility of 15 cm$^2$ V$^{-1}$ s$^{-1}$ at 1.7 K. The results of this work will facilitate further exploration of the magneto-electric effects and gate-tunable properties of $NiI_2$, including the incorporation of $NiI_2$ into heterostructures with other van der Waals materials. Since the methodology demonstrated here can be broadly applied to other ambient-reactive 2D materials, it has the potential to enable electrical interrogation of diverse magnetic, quantum, and spintronic phenomena at the atomically thin limit.

## 4. Experimental Section

*$NiI_2$ Crystal Growth and Exfoliation on $SiO_2$/Si*: $NiI_2$ crystals were grown by the chemical vapor transport method.[18] A stoichiometric amount of nickel (99.99%, 200-mesh) and iodine (99.99%) powders were sealed in a quartz ampoule (15 mm × 250 mm, <$10^{-3}$ Torr) that was placed in a horizontal tube furnace. The reaction mixture was heated to 750 °C for 5 days, while the cold end of the ampoule was held at room temperature. The $NiI_2$ crystals were removed from the ampoule and stored in an inert nitrogen atmosphere glovebox ($O_2$ and $H_2O$ < 0.1 ppm). Using Scotch tape, few-layer flakes were micromechanically exfoliated from the bulk crystal onto 300 nm $SiO_2$/Si substrates inside the inert nitrogen atmosphere glovebox. The thickness of few-layer $NiI_2$ on $SiO_2$/Si was identified based on optical contrast (red color channel, Figure S1, Supporting Information) and verified using inert-atmosphere atomic force microscopy (Figure 1).

*Atomic Force Microscopy*: An Asylum Cypher atomic force microscope with a Si cantilever (resonant frequency ≈320–340 kHz) was used for all atomic force microscopy analysis. The image resolution was 512 × 512 pixels at a scanning rate of 1.0–1.5 Hz. The images were all taken in a sealed UHP argon environmental cell.

*Ultrahigh Vacuum Scanning Tunneling Microscopy*: Room-temperature UHV-STM measurements ($10^{-10}$ Torr) were performed on a homebuilt STM with a Lyding-type scanner[31] interfaced with a SPECS Nanonis controller. Mechanically cut Pt-Ir tips (Bruker) were used for the measurements. Single-crystal $NiI_2$ was used for the UHV-STM measurements. To avoid ambient exposure, the $NiI_2$ crystal was mounted on the STM sample holder in a $N_2$ glovebox and transferred to the load-lock of the UHV chamber using a custom-made transfer flask. $NiI_2$ was cleaved in UHV to expose a fresh crystal surface prior to STM characterization.

*Raman, Photoluminescence, and Absorption Spectroscopies*: Raman and photoluminescence spectroscopies were conducted using a Horiba XPloRA confocal setup (532 nm laser with a spot size of ≈1 um with a 100× objective). For absorption spectroscopy (Cary-5000 UV/Vis Spectrophotometer with an integration sphere), $NiI_2$ was exfoliated on sapphire. All measurements were performed after alumina ALD to encapsulate the flakes and prevent ambient degradation.

*Device Fabrication*: Device fabrication was performed by combining polymer-assisted flake pick-up and clean-room lithography methods. Flake pick-up and transfer were performed using a 2D crystal manipulation system (Graphene Industries) located in the nitrogen glovebox. To prepare the polymer stamp, a dome of polydimethylsiloxane (PDMS) was first prepared on a glass slide by curing a droplet of the PDMS curing agent and base mixture (1:10). Next, a film of poly(bisphenol A carbonate) (PC, Sigma–Aldrich) was prepared by doctor-blading a solution of PC in chloroform, which was then stretched over the PDMS dome using Scotch tape. The resulting PC/PDMS stamp was heated on a hot plate at 120 °C for 10 min. Hexagonal boron nitride (hBN) and graphite were exfoliated onto $SiO_2$/Si using Scotch tape, and flakes of desired thickness and size were identified prior to device assembly. Device assembly was started by picking up the top hBN flake, followed by sequential pick-up of other flakes, and landing the heterostructure on prepatterned metal contacts by melting the PC at a temperature exceeding 150 °C. The prepatterned metal contacts on 300 nm thick $SiO_2$/Si substrates were fabricated using a Maskless Aligner (Heidelberg MLA150) with positive resist followed by reactive ion etching (Samco RIE-10NR) and metal evaporation.

Hall bar devices were fabricated by first picking up two or three few-layer graphene flakes with the top hBN flake (which defines the area for the $NiI_2$ flake), followed by pick up of the $NiI_2$ flake and bottom hBN. The stack was then patterned (electron-beam lithography, FEI Quanta 600F) and etched via reactive-ion etching. A thick poly(methyl methacrylate) (PMMA, A8 950) resist (≈1 µm) prepared by spin coating at a rate of 4000 rpm was used for electron-beam lithography. Since reactive ion etching exposes the edges of the $NiI_2$ flake, the devices were quickly moved into a metallic vessel and evacuated (<10 s of ambient exposure), followed by transfer into the inert-atmosphere glovebox. Resist stripping was performed in the glovebox using air-free and water-free 1,2-dichloroethane (1,2-DCE), followed by masking the metal contacts with Kapton tape and encapsulating the device structure via atomic layer deposition of alumina (Anric AT 400).

*Sequential Flake Removal*: A polymer stamp of PC/PDMS was brought into contact with the substrate/$NiI_2$ flakes at 100 °C. The substrate was heated to 130 °C with careful control of the PC contact front to prevent any contact with the few-layer sample while maximizing contact with the thicker flakes. After leaving the PC stamp in contact with the flakes of interest for a few minutes following turn off of the heater, the PC film was slowly detached from the surface, thus tearing off the undesired bulk $NiI_2$ flakes.

*Reactive Ion Etching*: Reactive ion etching was used to fabricate prepatterned metal contacts and to etch the devices to the Hall bar shape. For the prepatterned metal contacts, the etching of $SiO_2$ prior to metal evaporation was performed using $CF_4$ gas (20 sccm, 3.3 Pa, 100 W, etch rate 0.5 nm $s^{-1}$) using a Samco RIE-10NR instrument. Etching of the van der Waals heterostructures was performed in two steps: top hBN was etched with $CF_4$ (20 sccm, 3.3 Pa, 100 W, etch rate 2.6 nm $s^{-1}$) and the rest of the stack ($NiI_2$, graphene) was etched with Ar plasma (20 sccm, 3.3 Pa, 60 W, 2–4 min).

*Atomic Layer Deposition*: Alumina was grown in a commercial Anric AT 400 ALD reactor using alternating pulses of trimethyl aluminum (TMA, Sigma–Aldrich) and water. The ALD reactor is connected to a nitrogen glovebox ($O_2$ and $H_2O$ < 1 ppm) to load samples without ambient exposure. The ALD growth was performed at 100 °C for 500 cycles, which corresponds to ≈55 nm of alumina.

*Electrical Transport and Bulk Photovoltaic Effect Measurements*: Device measurements were performed in a Lakeshore CRX 4K and Lakeshore CRX-VF probe stations, variable-temperature cryostat (Attocube AttoDRY2100), and Dynacool PPMS (Quantum Design). The devices were wire-bonded to the chip carriers using a homebuilt In-Au bonder. Keithley Source Meter 2400 units and a Keithley Nanovoltmeter 2182 unit were used to probe charge transport.

Bulk photovoltaic effect measurements were performed using a Lakeshore CRX-VF probe station (with a custom lid allowing for use of magnifying optics) and a SuperK Extreme EXR-20 laser (NKT Photonics) at 530 nm (LLTF-VIS monochromator) at a power of 100 µW. The laser was modulated with a mechanical chopper before being linearly polarized and focused on the channel of the device using a long working distance 50× objective. The signal was detected using an SR830 lock-in amplifier (Stanford Research).

*Second Harmonic Generation and Linear Dichroism Measurements*: All low-temperature optical measurements were carried out with samples mounted in a closed cycle variable temperature cryostat. Second harmonic generation measurements were performed using a Ti:sapphire laser with a pulse repetition rate of 76 MHz and pulse width of 150 fs. The 1.49 eV output from the laser was focused onto the sample with a long working distance 50× objective using a homebuilt microscope setup. The second harmonic generation signal was collected in reflection geometry and directed to a spectrometer with an Andor CCD camera for detection.

Linear dichroism measurements were performed using a CW 2.33 eV laser. The laser was modulated with a mechanical chopper before being linearly polarized and sent through a photo-elastic modulator (PEM). The PEM was set to have a maximum retardance of $0.5\lambda$ with a fast axis at 45 degrees with respect to the input polarization. A half waveplate was used to rotate the modulated polarization with respect to the crystal axes before being focused onto the sample with a 100× objective. The linear dichroism signal was collected in reflection geometry and directed to a Thorlabs avalanche photodiode for lock-in detection.

## Supporting Information

Supporting Information is available from the Wiley Online Library or from the author.

## Acknowledgements

This research was primarily supported by the National Science Foundation Division of Materials Research (NSF DMR-2004420). In addition, D.L. acknowledges support from the Swiss National Science Foundation for an Early PostDoc Mobility Fellowship (P2EZP2_181614) and the Materials Research Science and Engineering Center of Northwestern University (NSF DMR-1720139) for charge transport measurements. H.Y.P. acknowledges support from the Department of Energy (DOE DE-SC0019356) for UHV-STM characterization, and E.S.G. acknowledges support from the National Science Foundation Division of Materials Research (NSF DMR-1905986) for variable-temperature cryostat measurements. K.W. and T.T. acknowledge support from JSPS KAKENHI (Grant Numbers 19H05790, 20H00354, and 21H05233) for hBN synthesis. This work made use of the Northwestern University NUANCE Center and the Northwestern University Micro/Nano Fabrication Facility (NUFAB), which have received support from the SHyNE Resource (NSF ECCS-1542205), the International Institute for Nanotechnology, and the Northwestern University MRSEC program (NSF DMR-1720139). This work also utilized the Northwestern University Magnet, Low Temperature, and Optical Facility, which is supported by the Northwestern University MRSEC program (NSF DMR-1720139). The Lakeshore CRX-VF probe station, SuperK Extreme EXR-20 laser (NKT Photonics), and 2D crystal manipulation system (Graphene Industries) used in this work were supported by an Office of Naval Research DURIP grant (ONR N00014-19-1-2297).

## Conflict of Interest

The authors declare no conflict of interest.

## Author Contributions

D.L. and J.T.G. contributed equally to this work. D.L., J.T.G., and M.C.H. devised the principal objectives of the project. D.L. grew the $NiI_2$ crystals by chemical vapor transport method. J.T.G., D.L., J.C., L.G., and T.W.S. exfoliated the $NiI_2$ flakes for optical measurements and fabricated the electrical devices. L.G. performed atomic force microscopy measurements. H.Y.P. performed scanning tunneling microscopy measurements. D.L. and J.T.G. performed the magnetotransport measurements with the help of E.S.G. and T.K.S. under the supervision of V.K.S. E.S.G. performed low-temperature optical measurements under the supervision of N.P.S. K.W. and T.T. provided the hBN crystals. M.C.H. supervised the project. D.L., J.T.G., and M.C.H. wrote the manuscript with input from all authors.

## Data Availability Statement

The data that support the findings of this study are available from the corresponding author upon reasonable request.

## Keywords

2D magnets, 2D multiferroicity, 2D semiconductors, band-like transport, helical antiferromagnets

Received: October 29, 2022
Published online: January 12, 2023

[1] H. Kurebayashi, J. H. Garcia, S. Khan, J. Sinova, S. Roche, *Nat Rev Phys* **2022**, *4*, 150.
[2] H. Li, S. Ruan, Y. J. Zeng, *Adv. Mater.* **2019**, *31*, 1900065.
[3] C. J. Cui, W. J. Hu, X. G. Yan, C. Addiego, W. P. Gao, Y. Wang, Z. Wang, L. Z. Li, Y. C. Cheng, P. Li, X. X. Zhang, H. N. Alshareef, T. Wu, W. G. Zhu, X. Q. Pan, L. J. Li, *Nano Lett.* **2018**, *18*, 1253.
[4] K. Chang, J. Liu, H. Lin, N. Wang, K. Zhao, A. Zhang, F. Jin, Y. Zhong, X. Hu, W. Duan, Q. Zhang, L. Fu, Q. K. Xue, X. Chen, S. H. Ji, *Science* **2016**, *353*, 274.

[5] Z. Y. Fei, W. J. Zhao, T. A. Palomaki, B. S. Sun, M. K. Miller, Z. Y. Zhao, J. Q. Yan, X. D. Xu, D. H. Cobden, *Nature* **2018**, *560*, 336.
[6] B. Huang, G. Clark, E. Navarro-Moratalla, D. R. Klein, R. Cheng, K. L. Seyler, D. Zhong, E. Schmidgall, M. A. McGuire, D. H. Cobden, W. Yao, D. Xiao, P. Jarillo-Herrero, X. Xu, *Nature* **2017**, *546*, 270.
[7] T. P. Kaloni, K. Chang, B. J. Miller, Q. K. Xue, X. Chen, S. H. Ji, S. S. P. Parkin, S. Barraza-Lopez, *Phys. Rev. B* **2019**, *99*, 134108.
[8] B. Huang, G. Clark, D. R. Klein, D. MacNeill, E. Navarro-Moratalla, K. L. Seyler, N. Wilson, M. A. McGuire, D. H. Cobden, D. Xiao, W. Yao, P. Jarillo-Herrero, X. Xu, *Nat. Nanotechnol.* **2018**, *13*, 544.
[9] S. Jiang, J. Shan, K. F. Mak, *Nat. Mater.* **2018**, *17*, 406.
[10] T. Song, X. Cai, M. W. Tu, X. Zhang, B. Huang, N. P. Wilson, K. L. Seyler, L. Zhu, T. Taniguchi, K. Watanabe, M. A. McGuire, D. H. Cobden, D. Xiao, W. Yao, X. Xu, *Science* **2018**, *360*, 1214.
[11] T. Jungwirth, X. Marti, P. Wadley, J. Wunderlich, *Nat. Nanotechnol.* **2016**, *11*, 231.
[12] F. Wu, I. Gutierrez-Lezama, S. A. Lopez-Paz, M. Gibertini, K. Watanabe, T. Taniguchi, F. O. von Rohr, N. Ubrig, A. F. Morpurgo, *Adv. Mater.* **2022**, *34*, 2109759.
[13] N. Mounet, M. Gibertini, P. Schwaller, D. Campi, A. Merkys, A. Marrazzo, T. Sohier, I. E. Castelli, A. Cepellotti, G. Pizzi, N. Marzari, *Nat. Nanotechnol.* **2018**, *13*, 246.
[14] J. B. Wu, H. Y. Chen, N. Yang, J. Cao, X. D. Yan, F. X. Liu, Q. B. Sun, X. Ling, J. Guo, H. Wang, *Nat. Electron.* **2020**, *3*, 466.
[15] H. Liu, X. Wang, J. Wu, Y. Chen, J. Wan, R. Wen, J. Yang, Y. Liu, Z. Song, L. Xie, *ACS Nano* **2020**, *14*, 10544.
[16] M. P. Pasternak, R. D. Taylor, A. Chen, C. Meade, L. M. Falicov, A. Giesekus, R. Jeanloz, P. Y. Yu, *Phys. Rev. Lett.* **1990**, *65*, 790.
[17] T. Kurumaji, S. Seki, S. Ishiwata, H. Murakawa, Y. Kaneko, Y. Tokura, *Phys. Rev. B* **2013**, *87*, 014429.
[18] S. R. Kuindersma, J. P. Sanchez, C. Haas, *Physica B Condens Matter* **1981**, *111*, 231.
[19] Q. Song, C. A. Occhialini, E. Ergecen, B. Ilyas, D. Amoroso, P. Barone, J. Kapeghian, K. Watanabe, T. Taniguchi, A. S. Botana, S. Picozzi, N. Gedik, R. Comin, *Nature* **2022**, *602*, 601.
[20] S. Son, Y. Lee, J. H. Kim, B. H. Kim, C. Kim, W. Na, H. Ju, S. Park, A. Nag, K. J. Zhou, Y. W. Son, H. Kim, W. S. Noh, J. H. Park, J. S. Lee, H. Cheong, J. H. Kim, J. G. Park, *Adv. Mater.* **2022**, *34*, 2109144.
[21] Y. An, H. Wang, J. Liao, Y. Gao, J. Chen, Y. Wu, Y. Li, G. Xu, C. Ma, *Phys. E Low Dimens. Syst. Nanostruct.* **2022**, 115262.
[22] J. T. Gish, D. Lebedev, T. K. Stanev, S. Jiang, L. Georgopoulos, T. W. Song, G. Lim, E. S. Garvey, L. Valdman, O. Balogun, Z. Sofer, V. K. Sangwan, N. P. Stern, M. C. Hersam, *ACS Nano* **2021**, *15*, 10659.
[23] D. A. Bandurin, A. V. Tyurnina, G. L. Yu, A. Mishchenko, V. Zólyomi, S. V. Morozov, R. K. Kumar, R. V. Gorbachev, Z. R. Kudrynskyi, S. Pezzini, Z. D. Kovalyuk, U. Zeitler, K. S. Novoselov, A. Patanè, L. Eaves, I. V. Grigorieva, V. I. Fal'Ko, A. K. Geim, Y. Cao, *Nat. Nanotechnol.* **2017**, *12*, 223.
[24] T. Kurumaji, S. Seki, S. Ishiwata, H. Murakawa, Y. Kaneko, Y. Tokura, *Phys. Rev. B* **2013**, *87*, 014429.
[25] H. Ju, Y. Lee, K. T. Kim, I. H. Choi, C. J. Roh, S. Son, P. Park, J. H. Kim, T. S. Jung, J. H. Kim, K. H. Kim, J. G. Park, J. S. Lee, *Nano Lett.* **2021**, *21*, 5126.
[26] P. Majumdar, P. B. Littlewood, *Nature* **1998**, *395*, 479.
[27] E. J. Telford, A. H. Dismukes, K. Lee, M. Cheng, A. Wieteska, A. K. Bartholomew, Y. S. Chen, X. Xu, A. N. Pasupathy, X. Zhu, C. R. Dean, X. Roy, *Adv. Mater.* **2020**, *32*, 2003240.
[28] G. Tenasini, E. Martino, N. Ubrig, N. J. Ghimire, H. Berger, O. Zaharko, F. Wu, J. F. Mitchell, I. Martin, L. Forró, A. F. Morpurgo, *Phys. Rev. Res.* **2020**, *2*, 023051.
[29] A. O. Fumega, J. L. Lado, *2D Mater.* **2022**, *9*, 025010.
[30] B. W. Baugher, H. O. Churchill, Y. Yang, P. Jarillo-Herrero, *Nano Lett.* **2013**, *13*, 4212.
[31] E. T. Foley, N. L. Yoder, N. P. Guisinger, M. C. Hersam, *Rev. Sci. Instrum.* **2004**, *75*, 5280.